Article

Trimetallic Pd@Pt_xAu_{1-x} Core-Shell Nanocubes with Enhanced Selectivity toward H_2O_2 for the Oxygen Reduction Reaction

Zhiqi Wang [1], Kei Kwan Li [1], Yong Ding [2], and Younan Xia [1,3,*]

[1] School of Chemistry and Biochemistry, Georgia Institute of Technology, Atlanta, GA 30332, USA
[2] School of Materials Science and Engineering, Georgia Institute of Technology, Atlanta, GA 30332, USA
[3] The Wallace H. Coulter Department of Biomedical Engineering, Georgia Institute of Technology and Emory University, Atlanta, GA 30332, USA
* Correspondence: younan.xia@bme.gatech.edu

Received: 10 October 2025; Revised: 30 October 2025; Accepted: 7 November 2025; Published: 13 November 2025

Abstract: We report a versatile method based on seed-mediated growth for the facile synthesis of trimetallic Pd@Pt_xAu_{1-x} core-shell nanocubes. By simply varying the feeding ratio between the Pt(II) and Au(III) precursors, the atomic ratio of Pt to Au in the shell and thereby the ensemble state of Pt atoms on the surface can be tuned to control the binding configuration of O_2 molecules. Specifically, discrete Pt atoms on the surface promote the adsorption of O_2 molecules in the Pauling configuration to enhance the catalytic selectivity of the nanoparticles toward H_2O_2 via the two-electron oxygen reduction reaction, with the Pd@$Pt_{0.025}Au_{0.975}$ nanocubes showing selectivity as high as 91% at 0.45 V_{RHE}. This work offers a viable means to augment the electrocatalytic performance of alloy nanocrystals by controlling their surface compositions.

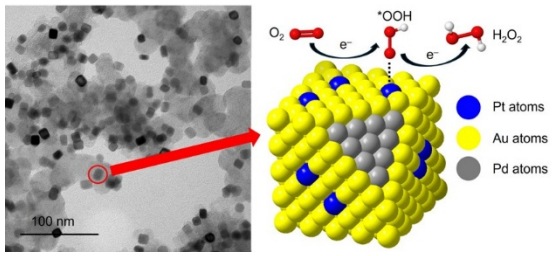

Keywords: alloy nanocrystals; core-shell nanocubes; H_2O_2 selectivity; oxygen reduction reaction; seed-mediated growth

1. Introduction

Electrochemical production of industrially valuable chemicals offers a viable way to fight the ever-increasing global climate crisis [1]. To this end, electrochemical synthesis of hydrogen peroxide (H_2O_2), a reagent widely used in healthcare, chemical synthesis, and paper bleaching sectors [2], has received great interest in recent years due to its reduced production of wastes and potentially lower cost than the commercial anthraquinone oxidation process [3]. Specifically, the oxygen reduction reaction (ORR) offers a promising route to the electrochemical production of H_2O_2. The success of this process critically depends on the availability of an electrocatalyst with high selectivity toward H_2O_2 because of the two competing pathways that involve two and four electrons ($2e^-$ vs. $4e^-$), respectively, to produce H_2O_2 and H_2O [3–5].

Various types of electrocatalysts have been explored to achieve $2e^-$ ORR [6–8], among which Pt- and Pd-based nanocrystals have proven to be the most successful candidates as they exhibit high activity toward ORR. In a prior study, our group developed a synthesis of bimetallic Pd@Pd_xAu_{1-x} core-shell nanocubes and demonstrated variation of Pd to Au ratio as an effective way to enhance selectivity toward $2e^-$ ORR [9]. In the present work, we seek to replace the Pd with Pt because the latter is known to have a higher activity toward ORR and has found commercial use in proton-exchange membrane fuel cells (PEMFCs) [10]. Similar to Pd, an extended surface made of Pt has a low selectivity toward $2e^-$ ORR [11], primarily due to the involvement of unfavorable intermediates. Specifically, the binding configuration of O_2 molecule has a direct impact on the type of intermediate and thus the ORR pathway. During ORR, O_2 molecules is expected to adsorb onto the metal surface to form *OOH (which then transforms to H_2O_2) or undergo O-O cleavage to generate *O. Typically, the adsorption of O_2 on a surface can take three different configurations: Pauling type (end-on coordination to one metal atom), Griffith type (side-on

coordination to one metal atom), and Yeager type (side-on bridge coordination to two adjacent metal atoms) [12]. Theoretical calculations suggest that the formation of *O species is thermodynamically favored on Pt{100} facets involving an array of touching Pt atoms [13,14]. As a result, it is critical to maintain Pt as discrete atoms on the surface to prevent the formation of *O species and thus augment the selectivity toward H_2O_2. To this end, coating the surface of a Pt catalyst with amorphous carbon was explored to limit the formation of large Pt ensembles and thus promote the Pauling type adsorption, enhancing the selectivity toward H_2O_2 [15]. Alloying Pt with another host metal has also proven to be effective in generating isolated Pt atoms on the surface [16]. In this approach, Siahrostami et al. have evaluated the performance of over 30 Pt-based alloys toward $2e^-$ ORR using density functional theory (DFT) calculation and identified $PtHg_4$ as a promising candidate [13]. However, the high toxicity of Hg limits the large-scale use of such catalysts. Alternatively, Brimaud et al. reported that the use of a Au-rich surface could shift the catalytic properties of Pt and thus increase its tendency toward H_2O_2 formation when tested with a model monolayer system [17]. Our previous work also demonstrated that co-deposition of Pd and Au atoms at different atomic ratios offered an effective means to improve the dispersity of Pd atoms on the surface and thus boost the selectivity toward $2e^-$ ORR [9].

Herein, we report the synthesis and characterizations of trimetallic Pd@Pt_xAu_{1-x} core-shell nanocubes with high selectivity toward H_2O_2 by controlling the ensemble state of Pt atoms on the surface. We synthesized Pd nanocubes by reducing Na_2PdCl_4 in an aqueous solution, followed by co-titration of an aqueous mixture of K_2PtCl_4 and $HAuCl_4$ to simultaneously deposit Pt and Au on the Pd seeds. The feeding ratio between the Pt(II) and Au(III) precursors can be conveniently varied to control the ensemble state of Pt atoms on the surface. For convenience, the products are denoted by the feeding molar ratio between the Pt(II) and Au(III) precursors. For example, the Pd@$Pt_{0.025}Au_{0.975}$ sample indicates that the molar ratio of Pt(II) to Au(III) precursors is set to 0.025:0.975 during the synthesis. Our results indicate that the Pd@$Pt_{0.025}Au_{0.975}$ nanocubes have high (over 75%) selectivity toward H_2O_2 in the potential range of 0.05–0.45 V_{RHE}, much augmented than the commercial Pt/C catalyst.

2. Materials and Methods

2.1. Chemicals and Materials

Sodium tetrachloropalladate (Na_2PdCl_4), potassium tetrachloro-platinate(II) (K_2PtCl_4), gold(III) chloride trihydrate ($HAuCl_4 \cdot 3H_2O$), L-ascorbic acid (AA), poly(vinyl pyrrolidone) (PVP, MW ≈ 55,000) and potassium bromide (KBr) were all obtained from Sigma-Aldrich (St. Louis, MO, USA) and used as received. Deionized (DI) water with a resistivity of 18.2 MΩ·cm at room temperature was used for all the experiments.

2.2. Synthesis of the 10-nm Pd Nanocubes Serving as Seeds

The nanocubes were synthesized according to our previously published protocol [18]. In a typical process, 105 mg of PVP (MW ≈ 55,000), 60 mg of AA, and 300 mg of KBr were dissolved in 8 mL of water, preheated at 80 °C for 30 min, and 3 mL of aqueous Na_2PdCl_4 (19 $mg \cdot mL^{-1}$) was added in one shot. The reaction was allowed to proceed for 3 h. The solid products were collected by centrifugation, washed twice with ethanol and once with water, and then dispersed in water for further use.

2.3. Synthesis of Pd@Pt_xAu_{1-x} Core-Shell Nanocubes

In a standard protocol, 66.5 mg of PVP (MW ≈ 55,000), 30 mg of AA and 19 mg of KBr were dissolved in 2.8 mL of water, and 0.3 mL of 10-nm Pd nanocubes was added as the seeds (1.34 $mg \cdot mL^{-1}$ as determined using ICP-MS). The mixture was preheated at 95 °C for 30 min. Different volumes of aqueous $HAuCl_4$ (40 mM) and aqueous K_2PtCl_4 (6.09 mM) were mixed in 10 mL of water. The specific volumes are 19 μL of aqueous $HAuCl_4$ for Pd@Au core-shell nanocubes, 18.52 μL of aqueous $HAuCl_4$ solution and 3.1 μL of aqueous K_2PtCl_4 for Pd@$Pt_{0.025}Au_{0.975}$, 18.05 μL of aqueous $HAuCl_4$ and 6.2 μL of aqueous K_2PtCl_4 for Pd@$Pt_{0.05}Au_{0.95}$, and 17 μL of aqueous $HAuCl_4$ and 12.4 μL of aqueous K_2PtCl_4 for Pd@$Pt_{0.1}Au_{0.9}$. For the synthesis of each sample, 4 mL of the mixture was injected into the reaction solution at a rate of 1 $mL \cdot h^{-1}$, and the reaction was allowed for another 10 min after the injection. The solid products were collected by centrifugation, washed twice with ethanol and once with water, and then dispersed in water for further use.

2.4. Characterizations

Transmission electron microscopy (TEM) images were taken using a Hitachi HT7700 microscope (Hitachi High-Technologies Corporation, Tokyo, Japan) operated at 120 kV. The elemental compositions of the samples

were determined using an inductively-coupled plasma mass spectrometer (ICP-MS, NexION 300 Q, PerkinElmer, Waltham, MA, USA). X-ray photoelectron spectroscopy (XPS) analyses were conducted using Thermo K-Alpha (Thermo Fisher Scientific, Waltham, MA, USA). Scanning transmission electron microscopy (STEM) images and energy- dispersive X-ray (EDX) spectroscopy data were acquired on a transmission electron microscope (FEI Tecnai F30 (FEI Company, Hillsboro, OR, USA; now part of Thermo Fisher Scientific)) equipped with a EDX detector. The high-angle annular dark-field scanning transmission electron microscopy (HAADF-STEM) images were captured using Hitachi HD 2700 (Hitachi High-Technologies Corporation, Tokyo, Japan) at an acceleration voltage of 200 kV. The samples for TEM analysis were prepared by drop casting the dispersions of nanoparticles on carbon-coated Cu grids, followed by drying under ambient conditions.

2.5. Preparation of a Working Electrode

The catalyst ink was prepared by mixing the as-prepared nanocrystals and carbon black (VXC72R, Cabot Corporation (Boston, MA, USA)) in ethanol under ultrasonication in an ice bath for 3 h. The carbon-supported catalyst was collected by centrifugation, and 1 mg of the catalyst was re-dispersed in 1 mL of water and isopropanol mixture (VH_2O/VIPA = 4/1) containing 10 μL Nafion (5% solution, Sigma-Aldrich). The metal contents in the ink were determined using ICP-MS. To benchmark the performance of Pd@Pt_xAu_{1-x}, a commercial Pt/C catalyst was used as the reference (3.2-nm Pt particles supported on Vulcan XC72, Premetek Co. (Cherry Hill, NJ, USA), with a Pt loading of 20 wt. %). The ink was prepared by mixing 2 mg of Pt/C, 1 mL of water, 1 mL of isopropanol, and 10 μL of Nafion under ultrasonication for 30 min. The working electrode was prepared by polishing with 0.3-μm Al_2O_3 slurry, washed with ethanol and water, and then polished by 0.05-μm Al_2O_3 slurry, followed by washing with ethanol and water. A proper amount of the suspension (10 μL) was deposited on a pre-cleaned glassy carbon rotating ring-disk electrode (RRDE, Pine Research Instrumentation (Durham, NC, USA)) with a geometric area of 0.237 cm^2 and then dried in air to give a total metal loading of around 2 μg.

2.6. Electrochemical Measurements

The electrochemical measurements were performed in a standard three-electrode cell using a WaveDriver 200 EIS Biopotentiostat electrochemical workstation. A standard size single junction Ag/AgCl reference electrode (+199 mV vs. NHE, PINE Research) and a Pt wire in a fritted isolation tube served as reference and counter electrodes. An aqueous $HClO_4$ solution (Baker) with a concentration of 0.1 M was used as an electrolyte. The catalyst was pre-cleaned by cycling between 0.05–1.20 V_{RHE} at a sweeping rate of 100 mV/s for 20 times. The cyclic voltammetry (CV) curve was then measured in an Ar-saturated electrolyte solution in the potential range of 0.05–1.00 V_{RHE} at a scan rate of 50 mV/s. The polarization curve was measured by the disk electrode for reducing oxygen and the ring electrode for oxidizing the hydrogen peroxide produced on the disk electrode. The linear sweep voltammetry (LSV) curve was measured at room temperature in the potential range of 0.05–1.00 V_{RHE} in an O_2-saturated electrolyte solution at 10 mV/s and a rotating speed of 1600 rpm. The collection efficiency (N) was 25.6% and the ring current was kept constant at 1.20 V_{RHE} to oxidize the hydrogen peroxide. The accelerated durability test (ADT) was performed by cyclic voltammetry in the potential range of 0.05–1.00 V_{RHE} in an O_2-saturated 0.1 M $HClO_4$ solution for 1000 cycles.

The H_2O_2 yield and electron transfer number for all samples were calculated using the following equations:

$$n = 4\, I_D/(I_D + I_R/N), \tag{1}$$

$$H_2O_2 \text{ Selectivity} = 200 \times 2\, I_R/[N \times (I_D + I_R/N)], \tag{2}$$

where I_R is the ring current, I_D is the disk current, N is the electron collection efficiency (25.6%), and n is the electron transfer number.

3. Results and Discussion

We began with the synthesis of Pd cubic seeds enclosed by {100} facets by reducing Na_2PdCl_4 in an aqueous solution at 80 °C, with ascorbic acid (AA) serving as a reductant [18]. Poly(vinyl pyrrolidone) (PVP) was also added as a colloidal stabilizer to prevent the nanocrystals from aggregation, together with the Br^- ions from KBr to selectively cap the {100} facets [19]. The Pd cubic seeds had an average edge length of 9.5 ± 1.5 nm (see Supplementary Materials Figure S1A). A syringe pump was then used to titrate an aqueous $HAuCl_4$ solution into the reaction mixture containing the Pd cubic seeds, AA, PVP, and KBr to generate Pd@Au core-shell nanocubes. As shown in Supplementary Materials Figure S1B, the average edge length of the core-shell nanocubes was increased to 11.8±1.4 nm, corresponding to a Au shell of ca. 1 nm in thickness, or 4–5 atomic layers. Supplementary Materials

Figure S1C shows a typical high-angle annular dark-field scanning transmission electron microscopy (HAADF-STEM) image of the core-shell nanocubes, confirming a shell thickness of about 4 atomic layers. The lattice spacing in the shell was measured to be 0.208 nm, consistent with the lattice spacing, 0.204 nm of (200) planes of face-centered cubic Au.

Incorporation of Pt atoms into the Au shell was achieved by titrating an aqueous mixture of K_2PtCl_4 and $HAuCl_4$ into the growth solution (see Supplementary Materials for details). Since the precursors were added dropwise, the reduction of Pt(II) and Au(III) precursors should undergo a steady state during the deposition process [20]. Therefore, the Pt:Au atomic ratio in each layer of the shell should be similar. Supplementary Materials Figure S2 shows TEM images of the Pd@Pt_xAu_{1-x} nanocubes with different Pt to Au atomic ratios denoted by the feeding molar ratio between the two precursors. Figure 1A shows a transmission electron microscopy (TEM) image of the Pd@$Pt_{0.025}Au_{0.975}$ core-shell nanocubes. Figure 1B shows energy-dispersive X-ray (EDX) spectroscopy line scans of a single nanocube along the red arrow in the inset. The outer region (in yellow color) exhibited stronger Au signals when compared to the inner region (in blue color), indicating that the Au atoms were confined to the shell. The presence of Pt signals confirmed the successful incorporation of Pt. Since only a trace amount of Pt was incorporated into the shell of this sample, the Pt signals were extremely low in intensity.

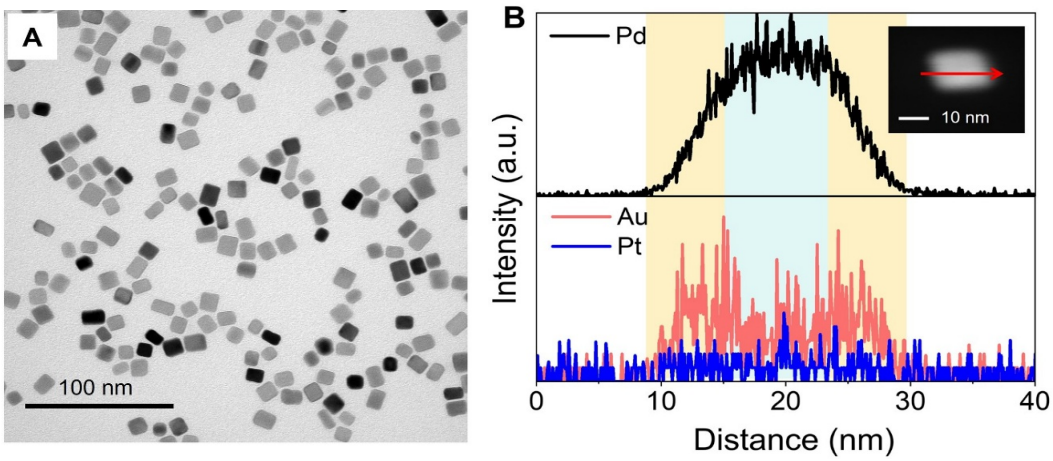

Figure 1. Characterizations of the Pd@$Pt_{0.025}Au_{0.975}$ core-shell nanocubes. (**A**) TEM image of the core-shell nanocubes and (**B**) EDX line scans along the red arrow on a STEM image shown in the inset.

To derive the average percentage of Pt in the shell, we conducted inductively-coupled plasma mass spectroscopy (ICP-MS) analysis of the sample and the data indicated that the Pt to Au atomic ratio in the shell was 0.001:0.999 (Supplementary Materials Table S1). The ICP-MS data also confirmed that with an increase in the feeding ratio between Pt(II) and Au(III) precursors from 0.025:0.975 to 0.1:0.9, the atomic ratio of Pt to Au in the shell also increased from 0.001:0.999 to 0.027:0.973. This trend implies that changing the feeding ratio of the precursors offers an effective means to tune the elemental composition of the shell. The difference between the feeding ratio and the exact atomic ratio determined by ICP-MS can be attributed to the variation in reduction rate between Pt(II) and Au(III) precursors during the synthesis. The X-ray photoelectron spectroscopy (XPS) data also confirmed the presence of Pt (Figure 2A). As expected, all the samples exhibited strong Pd 3d signals, together with Au 4f signals, as shown in Figure 2B,C, respectively. It should be noted that the position of the Au 4f peak was red-shifted due to the electron transfer between Au and Pt, and a detailed explanation will be given in the subsequent section. For the Pt 4f spectra (Figure 2D), the Pd@$Pt_{0.025}Au_{0.975}$ nanocubes did not show obvious Pt signals due to the extremely low amount of Pt in this sample. As the feeding ratio of Pt(II) to Au(III) precursors was increased, the Pt 4f peaks became more pronounced, consistent with the ICP-MS result. Notably, strong Br 3d peaks were observed (red dashed line), which could be attributed to the use of KBr in the synthesis and thus the chemisorption of Br^- ions on the {100} facets.

To prepare electrocatalysts, the core-shell nanocubes were loaded on carbon black by mixing in ethanol under ultrasonication. The particles maintained their cubic shape after ultrasonication, as shown by the TEM images in Supplementary Materials Figure S3B–D. We first obtained cyclic voltammetry (CV) curves of the different catalysts in an Ar-saturated 0.1 M $HClO_4$ solution after 20 cycles. As shown in Figure 3A, we observed the typical hydrogen adsorption/desorption peaks of Pt in the range of 0.10–0.30 V_{RHE}, as well as the negative Pt-O formation and removal peaks in the range of 0.50–0.80 V_{RHE} for all the samples [21]. We then evaluated the electrochemical performance of the different catalysts toward $2e^-$ ORR by measuring their polarization curves in the range of 0.05–1.00 V_{RHE}

in an O_2-saturated electrolyte solution using a rotation ring-disk electrode (RRDE). In this case, the disk electrode reduced oxygen while the ring electrode oxidized the H_2O_2 just formed on the disk electrode. We benchmarked the selectivity of the catalysts toward H_2O_2 against a commercial Pt/C catalyst. Figure 3B shows the polarization curves of different samples. The theoretical onset potential for $2e^-$ ORR is 0.70 V_{RHE} ($O_2+2H^++2e^- \rightarrow H_2O_2$ $E^\ominus$ = 0.70 V_{RHE}) [17]. For the commercial Pt/C catalyst, the onset potential was 0.94 V_{RHE}, indicating the dominance of the $4e^-$ ORR pathway. Compared to the other samples, the onset potentials of the Pd@$Pt_{0.05}Au_{0.95}$ and Pd@$Pt_{0.025}Au_{0.975}$ nanocubes were 0.60 V_{RHE} and 0.45 V_{RHE}, respectively, indicating the effective suppression of the $4e^-$ ORR pathway by alloying the Pt with Au. As shown by the results in Figure 3B, the catalytic performance of the Pd@Au nanocubes was relatively low compared to other samples containing Pt. This can be attributed to the involvement of different reaction intermediates. For the Pd@Au nanocubes, theoretical calculation has shown that the interaction between the Au{100} facets and O_2 molecules is weak and the rate-determining step (RDS) in ORR is the adsorption of the O_2 molecules [22,23], and the sluggish kinetics for the adsorption of O_2 molecules compromises the catalytic activity. Compared to Au, the interaction between Pt sites and O_2 molecules is much stronger, so the incorporation of Pt into the Au shell promotes the overall activity of ORR.

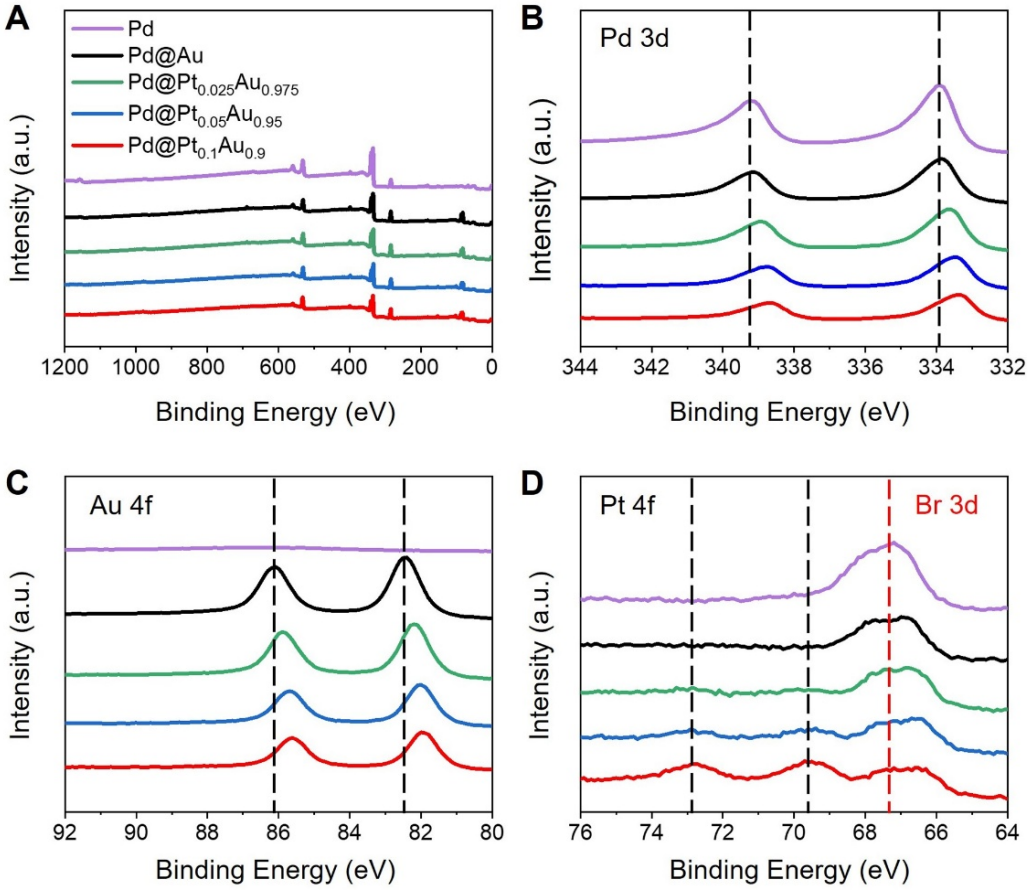

Figure 2. XPS spectra of the Pd cubic seeds and Pd@Pt_xAu_{1-x} core-shell nanocubes. (**A**) Survey spectra; (**B**) spectra of Pd 3d; (**C**) spectra of Au 4f; and (**D**) spectra of Pt 4f. The color scheme in (**A**) applies to all panels.

To further evaluate the catalytic performance, we calculated the selectivity toward H_2O_2 using Equation (1). As shown in Figure 3C, the selectivity toward $2e^-$ ORR for the commercial Pt/C catalyst (purple trace) was below 20%, primarily due to the preferential Yeager type adsorption of O_2 molecules on the surface of an extended Pt surface. In contrast, the selectivity of the Pd@$Pt_{0.1}Au_{0.9}$ nanocubes was increased to ca. 40%. The increase in selectivity relative to Pt/C confirmed that by decreasing the ratio of Pt to Au in the alloy shell, the adsorption mode of O_2 molecules could be switched from the Yeager to the Pauling type, promoting $2e^-$ ORR. Additionally, when the feeding ratio between Pt(II) and Au(III) precursors was reduced from 0.1:0.9 to 0.025:0.975, the selectivity was increased from 40% to 80% in the range of 0.20–0.45 V_{RHE}. Significantly, the selectivity of the Pd@$Pt_{0.025}Au_{0.975}$ nanocubes toward H_2O_2 production could be maintained over 77% in the range of 0.05–0.45 V_{RHE}, together with a maximum value of 91% at 0.45 V_{RHE}. This increase in selectivity could be ascribed to the favorable Pt ensembles state in the alloy shell. In general, the Au atoms in the alloy can lengthen the average Pt-Pt distance, boosting Pauling-type adsorption for the O_2 molecules and thus promoting the selectivity toward H_2O_2.

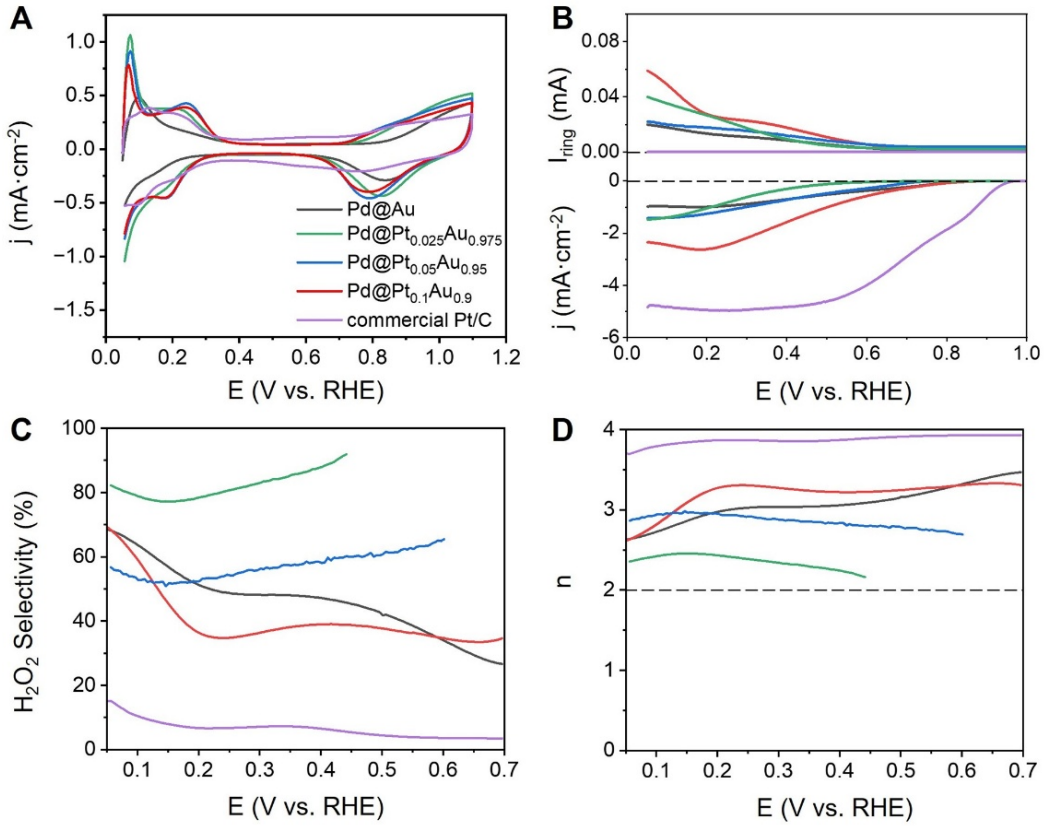

Figure 3. Electrocatalytic measurements of the Pd@Pt_xAu_{1-x} nanocubes and commercial Pt/C catalyst. (**A**) Cyclic voltammograms in an Ar-saturated 0.1 M $HClO_4$ solution; (**B**) polarization curves recorded using RRDE in an O_2-saturated 0.1 M $HClO_4$; (**C**) comparison of H_2O_2 selectivity; and (**D**) comparison of electron transfer number n. The color scheme in (**A**) applies to all panels.

We also calculated the electron transfer number (*n*) during ORR using Equation (2). As shown in Figure 3D, the electron transfer number of the commercial Pt/C catalyst was above 3.5 in the range of 0.05–0.70 V_{RHE}, implying the dominance of the 4e⁻ ORR pathway. In contrast, the value dropped to ca. 3 for Pd@$Pt_{0.05}Au_{0.95}$ and Pd@$Pt_{0.1}Au_{0.9}$ nanocubes, suggesting that there was a mixing in pathway between 2e⁻ and 4e⁻ ORR. For the Pd@$Pt_{0.025}Au_{0.975}$ nanocubes, the electron transfer number was close to 2, indicating the dominance of the 2e⁻ ORR pathway. Overall, the calculated electron transfer numbers were consistent with their selectivity toward H_2O_2.

The catalytic performance was found to be related to the electronic state of elements in the nanocrystals. To further understand the mechanism behind, a detailed analysis of XPS peaks of all the samples is summarized in Table S2. For the Pd@Au nanocubes, the Au 4f spectrum had peaks at 86.1 and 82.4 eV, corresponding to Au 4f5/2 and 4f7/2, respectively. Interestingly, increasing the amount of Pt in the Au shell to $Pt_{0.025}Au_{0.975}$ red-shifted the Au 4f peaks to 85.9 and 82.2 eV, respectively. The red shifts could be ascribed to an increase in electron density for Au. Since Au is more electronegative than Pt (electronegativity: Au/2.54 and Pt/2.28), there was a net charge transfer from Pt atoms to Au atoms. For 2e⁻ ORR, the direct binding between Pt and O_2 molecules was strong, making the desorption of *OOH to form H_2O_2 the rate-determining step. The charge transfer from Pt atoms to Au atoms leads to the decrease of electron density on Pt, thereby weakening the interaction between Pt and intermediate *OOH, as well as reducing the activation energy for the rate-determining step [24–26]. As a result, the 2e⁻ ORR pathway was preferred and hence the augmentation in selectivity toward H_2O_2.

We further evaluated the stability of the Pd@$Pt_{0.025}Au_{0.975}$ nanocubes through an accelerated durability test (ADT) by applying continuous cycling for up to 1000 cycles between 0.05–1.00 V_{RHE} in an O_2-saturated 0.1 M $HClO_4$ solution. Figure 4A,B, shows the selectivity toward H_2O_2 and the electron transfer number of the sample before and after ADT, respectively. After ADT, the selectivity toward H_2O_2 dropped to below 40% while the electron transfer number increased to ca. 4. This result indicates possible changes to surface composition and/or particle shape during the ADT process. Figure 4C,D, shows HAADF-STEM images of the Pd@$Pt_{0.025}Au_{0.975}$ nanocubes after 1000 cycles of ADT. The project profiles of the nanocubes became rounded, implying that their corners and edges were truncated during ADT. Such truncations could be attributed to the potential surface reconstruction of atoms, leading to the formation of Pd-Au-Pt alloy, which was supposed to be thermodynamically

more favorable [27]. This alloying effect would push the Pd atoms to the surface of the particle, promoting the Yeager type adsorption of O_2 molecules and thus compromising the selectivity toward $2e^-$ ORR.

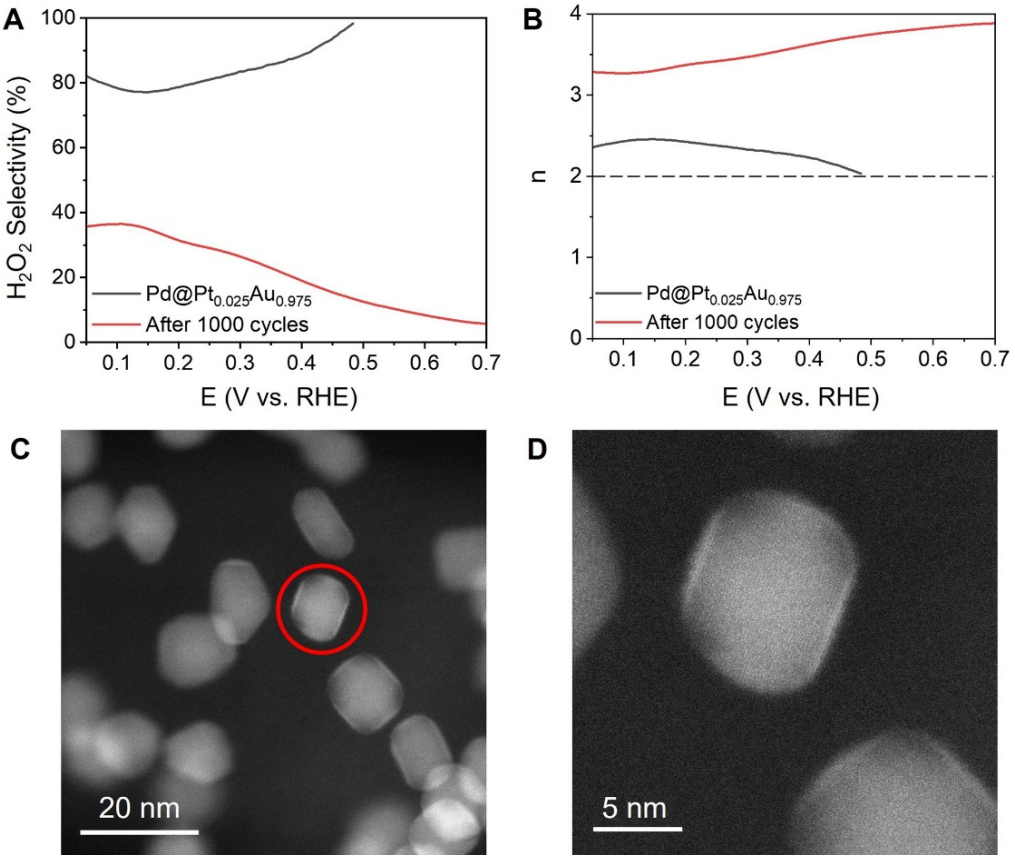

Figure 4. Stability test of the Pd@$Pt_{0.025}Au_{0.975}$ nanocubes. (**A**) Selectivity toward H_2O_2 in an O_2-saturated 0.1 M $HClO_4$ solution before and after 1000 cycles of ADT; (**B**) electron transfer number (n) before and after 1000 cycles of ADT; (**C**) HAADF-STEM image of the Pd@$Pt_{0.025}Au_{0.975}$ nanocubes after 1000 cycles of ADT; (**D**) enlarged image of a single Pd@$Pt_{0.025}Au_{0.975}$ nanocube marked by red circle in (**C**) with truncated corners. The color scheme in (**A**) also applies to panel (**B**).

5. Conclusions

In summary, controlling the ensemble state of Pt atoms in the surface of core-shell nanoparticles has been demonstrated as an effective means to regulate the reaction pathway in ORR and thereby boost the selectivity toward H_2O_2. The control could be readily achieved by changing the feeding ratio between the Pt(II) and Au(III) precursors during the synthesis. The synthesis has proven to be effective in producing a series of Pd@Pt_xAu_{1-x} core-shell nanocubes with different Pt to Au atomic ratios in the shell, and thus different Pt ensemble states on the surface. The electrocatalytic measurements further confirmed that all the samples exhibited high selectivity toward H_2O_2 production in ORR when compared to the commercial Pt/C catalyst. The synthetic approach is potentially extendible to other types of nanomaterials sought for various applications [28–30].

Supplementary Materials: The following supporting information can be downloaded at: https://media.sciltp.com/articles/others/2511131438558612/MI-25100042-Supplementary-Materials-FC-done.pdf, Figure S1: Synthesis of Pd and Pd@Au core-shell nanocubes; Figure S2: Variation of the feeding molar ratio between the Pt and Au precursors. TEM image of Pd@Pt_xAu_{1-x} core-shell nanocubes obtained with the different Pt:Au precursor molar ratio; Figure S3: TEM image of catalyst inks; Table S1: The Pt:Au atomic ratio in Pd@Pt_xAu_{1-x} nanocubes as derived from ICP-MS data; Table S2: Summary of the XPS peak position (unit: eV) of Pd and core-shell nanocubes.

Author Contributions: Y.X.: conceived the concept; Z.W.: conducted experiments on materials preparation, electrochemical measurements and analyzed the data; Y.D.: contributed to materials characterization; K.K.L.: conducted experiments on ICP measurements; Z.W. and K.K.L.: prepared the manuscript and Y.X.: revised the writing. All authors have read and agreed to the published version of the manuscript.

Funding: This work was supported in part by a grant from NSF (DMR-2333595) and start-up funds from the Georgia Institute of Technology.

Data Availability Statement: The dataset generated and/or analyzed during the current study are available from the corresponding author on reasonable request.

Conflicts of Interest: The authors declare no conflict of interest. Given the role as Editor-in-Chief, Younan Xia was not involved in the peer review of this paper and had no access to information regarding its peer-review process. Full responsibility for the editorial process of this paper was delegated to another editor of the journal..

Use of AI and AI-Assisted Technologies: No AI tools were utilized for this paper.

References

1. Luna, P.D.; Hahn, C.; Higgins, D.; Jaffer, S.A.; Jaramillo, T.F.; Sargent, E.H. What would it take for renewably powered electrosynthesis to displace petrochemical processes? *Science* **2019**, *364*, eaav3506.
2. Lewis, R.J.; Hutchings, G.J. Recent advances in the direct synthesis of H_2O_2. *ChemCatChem* **2019**, *11*, 298–308.
3. Siahrostami, S. H_2O_2 electrosynthesis and emerging applications challenges and opportunities: A computational perspective. *Chem Catal.* **2023**, *3*, 100568.
4. Shin, H.; Lee, S.; Sung, Y.-E. Industrial-scale H_2O_2 electrosynthesis in practical electrochemical cell systems. *Curr. Opin. Electrochem.* **2023**, *38*, 101224.
5. Wroblowa, H.S.; Pan, Y.-C.; Razumney, G. Electroreduction of oxygen: A new mechanistic criterion. *J. Electroanal. Chem*. **1976**, *69*, 195–201.
6. Shen, R.; Chen, W.; Peng, Q.; Lu, S.; Zheng, L.; Cao, X.; Wang, Y.; Zhu, W.; Zhang, J.; Zhuang, Z.; et al. High-concentration single atomic Pt sites on hollow CuS_x for selective O_2 reduction to H_2O_2 in acid solution. *Chem* **2019**, *5*, 2099–2110.
7. Zhang, J.; Ma, J.; Choksi, T.S.; Zhou, D.; Han, S.; Liao, Y.-F.; Yang, H.B.; Liu, D.; Zeng, Z.; Liu, W.; et al. Strong metal-support interaction boosts activity, selectivity and stability in electrosynthesis of H_2O_2. *J. Am. Chem. Soc*. **2022**, *144*, 2255–2263.
8. Shen, H.; Janes, A.N.; Ross, R.D.; Kaiman, D.; Huang, J.; Song, B.; Schmidt, J.R.; Jin, S. Stable and selective electrosynthesis of hydrogen peroxide and the electro-Fenton process on $CoSe_2$ polymorph catalysts. *Energy Environ. Sci*. **2020**, *13*, 4189–4203.
9. Zhang, Y.; Lyu, Z.; Chen, Z.; Zhu, S.; Shi, Y.; Chen, R.; Xie, M.; Yao, Y.; Chi, M.; Shao, M.; et al. Maximizing the catalytic performance of $Pd@Au_xPd_{1-x}$ nanocubes in H_2O_2 production by reducing shell thickness to increase compositional stability. *Angew. Chem. Int. Ed.* **2021**, *60*, 19643–19647.
10. Liu, M.; Zhao, Z.; Duan, X.; Huang, Y. Nanoscale structure design for high-performance Pt-based ORR catalysts. *Adv. Mater*. **2019**, *31*, 1802234.
11. Zhang, G.; Wei, Q.; Yang, X.; Tavares, A.C.; Sun, S. RRDE experiments on noble-metal and noble-metal-free catalysts: Impact of loading on the activity and selectivity of oxygen reduction reaction in alkaline solution. *Appl. Catal. B Environ*. **2017**, *206*, 115–126.
12. Gao, J.; Liu, B. Progress of electrochemical hydrogen peroxide synthesis over single atom catalysts. *ACS Mater. Lett*. **2020**, *2*, 1008–1024.
13. Siahrostami, S.; Verdaguer-Casadevall, A.; Karamad, M.; Deiana, D.; Malacrida, P.; Wickman, B.; Escudero-Escribano, M.; Paoli, E.A.; Frydendal, R.; Hansen, T.W.; et al. Enabling direct H_2O_2 production through rational electrocatalyst design. *Nat. Mater*. **2013**, *12*, 1137–1143.
14. Duan, Z.; Wang, G. Comparison of reaction energetics for oxygen reduction reactions on Pt(100), Pt(111), Pt/Ni(100) and Pt/Ni(111) surfaces: A first-principles study. *J. Phys. Chem. C* **2013**, *117*, 6284–6292.
15. Choi, C.H.; Kwon, H.C.; Yook, S.; Shin, H.; Kim, H.; Choi, M. Hydrogen peroxide synthesis via enhanced two-electron oxygen reduction pathway on carbon-coated Pt surface. *J. Phys. Chem. C* **2014**, *118*, 30063–30070.
16. Jiang, K.; Zhao, J.; Wang, H. Catalyst design for electrochemical oxygen reduction toward hydrogen peroxide. *Adv. Funct. Mater*. **2020**, *30*, 2003321.
17. Brimaud, S.; Engstfeld, A.K.; Alves, O.B.; Behm, R. Structure-reactivity correlation in the oxygen reduction reaction: Activity of structurally well-defined Au_xPt_{1-x}/Pt(111) monolayer surface alloys. *J. Electroanal. Chem*. **2014**, *716*, 71–79.
18. Jin, M.; Liu, H.; Zhang, H.; Xie, Z.; Liu, J.; Xia, Y. Synthesis of Pd nanocrystals enclosed by {100} facets and with sizes <10 nm for application in CO oxidation. *Nano Res*. **2011**, *4*, 83–91.
19. Peng, H.-C.; Xie, S.; Park, J.; Xia, X.; Xia, Y. Quantitative analysis of the coverage density of Br^- ions on Pd{100} facets and its role in controlling the shape of Pd nanocrystals. *J. Am. Chem. Soc*. **2013**, *135*, 3780–3783.
20. He, J.; Yu, H.; Xia, Y. Steady-state synthesis of colloidal metal nanocrystals. *Mater. Interfaces* **2025**, *2*, 213–225.
21. Duchesne, P.N.; Li, Z.Y.; Deming, C.P.; Fung, V.; Zhao, X.; Yuan, J.; Regier, T.; Aldalbahi, A.; Almarhoon, Z.; Chen, S.; et al. Golden single-atom-site platinum electrocatalysts. *Nat. Mater*. **2018**, *17*, 1033–1039.

22. Siahrostami, S.; Villegas, S.J.; Mostaghimi, A.H.B.; Back, S.; Farimani, A.B.; Wang, H.; Persson, K.A.; Montoya, J. A review on challenges and successes in atomic-scale design of catalysts for electrochemical synthesis of hydrogen peroxide. *ACS Catal*. **2020**, *10*, 7495–7511.
23. Mei, D.; He, Z.D.; Zheng, Y.L.; Jiang, D.C.; Chen, Y.-X. Mechanistic and kinetic implications on the ORR on a Au(100) electrode: pH, temperature and H-D kinetic isotope effects. *Phys. Chem. Chem. Phys.* **2014**, *16*, 13762–13773.
24. Ma, Z.; Cano, Z.P.; Yu, A.; Chen, Z.; Jiang, G.; Fu, X.; Yang, L.; Wu, T.; Bai, Z.; Lu, J. Enhancing oxygen reduction activity of Pt-based electrocatalysts: From theoretical mechanisms to practical methods. *Angew. Chem. Int. Ed*. **2020**, *59*, 18334–18348.
25. Kulkarni, A.; Siahrostami, S.; Patel, A.; Nørskov, J.K. Understanding catalytic activity trends in the oxygen reduction reaction. *Chem. Rev*. **2018**, *118*, 2302–2312.
26. Nørskov, J.K.; Rossmeisl, J.; Logadottir, A.; Lindqvist, L.; Kitchin, J.R.; Bligaard, T.; Josson, H. Origin of the overpotential for oxygen reduction at a fuel-cell cathode. *J. Phys. Chem. B* **2004**, *108*, 17886–17892.
27. Li, J.; Yin, H.-M.; Li, X.-B.; Okunishi, E.; Shen, Y.-L.; He, J.; Tang, Z.-K.; Wang, W.-X.; Yücelen, E.; Li, C.; et al. Surface evolution of a Pd-Pt-Au electrocatalyst for stable oxygen reduction. *Nat. Energy* **2017**, *2*, 17111–17116.
28. Yu, S.; Yang, H. One the surface composition of molybdenum carbide nanoparticles for electrocatalytic applications. *Mater. Interfaces* **2024**, *1*, 3–12.
29. Sun, W.; Min, B.; Wang, M.; Han, X.; Gao, Q.; Hwang, S.; Zhou, H.; Zhu, H. Catholic corrosion-induced structural evolution of CuNi electrocatalysts for enhanced CO_2 reduction. *Mater. Interfaces* **2024**, *1*, 79–88.
30. Zhou, J.; Shao, S.; Wei, Z.; Xia, X. Silver-platinum hollow nanoparticles for colorimetric lateral flow assay. *Mater. Interfaces* **2024**, *1*, 58–67.